ACS APPLIED MATERIALS & INTERFACES

www.acsami.org

Research Article

Selectively Confined Black Phosphorus Nanowires in Carbon Nanotubes

Yumin Da,[⊥] Xue Zhang,[⊥] Chao Peng,[⊥] Hao Huang, Shuai Zhang, Paul K. Chu, Xue-Feng Yu, and Jiahong Wang*

Cite This: *ACS Appl. Mater. Interfaces* 2023, 15, 54157−54165

Read Online

ACCESS | Metrics & More | Article Recommendations | Supporting Information

ABSTRACT: Nanoconfinement of low-dimensional materials opens up a new territory for tailoring material hybridization to produce novel geometric structures for applications in electronics, catalysis, and photonics. Despite the progress made in the encapsulation of 2D materials, exploration of their definite crystal structures into lower-dimensional nanomaterials is still largely unexplored. Herein, one-dimensional black phosphorus (BP) nanowires with an aspect ratio of over 100 produced by confining BP into the CNT (conf-BP@CNT) are reported. Notably, the unique structure and dimensions of BP were determined by confinement within the CNT and were accurately characterized by crystallography. During the spatially confined growth, the defects and capillarity effect of the CNT promote nucleation and growth of BP within the CNT. conf-BP@CNT shows surface charge localization of conf-BP and protection rendered by the CNT shell, giving rise to more efficient and stable photocatalytic rhodamine B (RhB) degradation than the bare exfoliated BP nanosheets. These results demonstrate the effectiveness of nanoconfinement in producing nanomaterials with controllable dimensions, precise spatial arrangement, and unique structures.

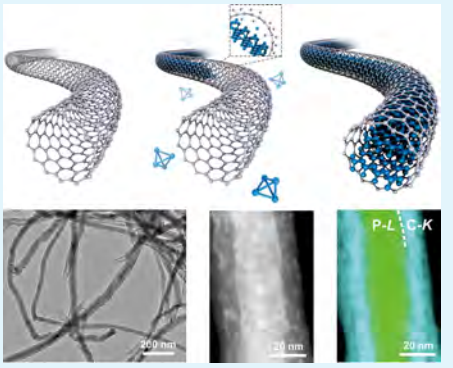

KEYWORDS: *black phosphorus, one-dimensional nanowire, confined growth, carbon nanotube, photocatalytic degradation*

INTRODUCTION

Shaping the precise geometry of two-dimensional (2D) materials on the nanoscale is crucial to expand their physicochemical properties. The dimension of nanomaterials dictates the properties and applications[1−3] because changes in the dimension can alter the symmetry of the state density, charge accumulation, polariton transmission, and exciton states.[4−6] Low-dimensional materials prepared by dimensional transformation including two-dimensional (2D) graphene[7] exfoliated from graphite and molybdenum sulfide (MoS_2) nanoribbons[8] etched from flakes have been proven to have large potential in microelectronics, catalysis, photonics, and other applications.[9] Limited by the large specific surface area and in-plane mechanical strength of 2D materials, the main effort of current research has still been for intrinsic 2D geometric modulation.[10,11] Complementary to 2D geometry, further exploring the transformation of 2D materials to lower-dimensional geometry, such as one-dimensional (1D) nanotubes[12] and nanowires,[13,14] is indispensable because such dimensional transformation predicted in theoretical calculation enables new opportunities for obtaining novel material properties and investigating interface reactions.[15−17] In particular, the assembly of 2D materials to form emerging 1D nanoscrolls[18] and high-order superlattices[19,20] yielded unique electronic and photonic properties, which have recently attracted considerable interest of researchers. However, the investigations of these 1D topological structures are strongly dependent on large available size and chemical inertness,[21,22] i.e., transition metal dichalcogenides (TMDs) and boron nitride (BN). Indeed, 2D materials with chemical activity and uncontrollable morphology, such as black phosphorus (BP), seem to be impossible to accomplish in terms of dimensional transformation in general.

Among the various dimension-transformation techniques, spatially confined growth is an effective strategy in which the arrangement of atoms and molecules on the proper templates or substrates can be tailored to produce specific structures.[23,24] In addition, materials prepared by spatial confinement can circumvent the limitations of traditional crystallography,[25,26] and more importantly, the interfacial interactions between the templates and confined structures can lead to new properties and functions.[27−31] Considering that the edge states of most 2D materials have attractive properties[32−36] and direct air exposure of BP leads to extensive oxidization,[37] spatially confined growth may be an ideal way to expand the functions

Received: August 25, 2023
Revised: October 26, 2023
Accepted: October 26, 2023
Published: November 9, 2023

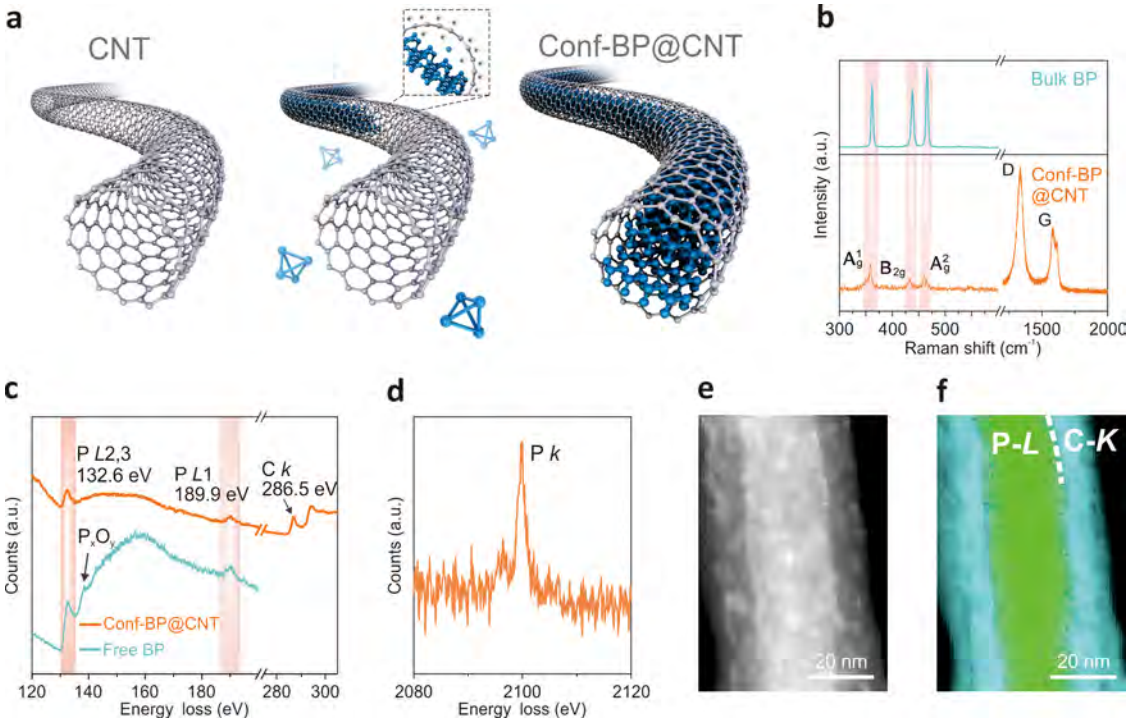

Figure 1. (a) Schematic diagram of spatially confined growth of 1D conf-BP@CNT. (b) Raman scattering spectra of conf-BP@CNT and bulk BP. (c) EELS spectra of conf-BP@CNT and free BP nanosheet. (d) P K-edge EELS spectrum of conf-BP@CNT. (e) HAADF-STEM image of conf-BP@CNT. (f) P $L_{2,3}$-edge (132.6 eV) and C K-edge (286.5 eV) of EELS mapping of (e).

of BP. For example, by confining BP into nanotubes, the conventional 2D BP would be transformed into a 1D coaxial nanowire, and the shell protects the inner BP, giving rise to new physicochemical effects. Although some phosphorus molecular chains have been embedded in carbon nanotubes, confined growth of BP with a complete crystal structure is still very challenging.[38−40]

Herein, a chemical vapor-phase transport (CVT) method is designed and demonstrated to selectively confine 2D BP (conf-BP) in multiwalled carbon nanotubes (CNTs). In this way, BP is converted into a continuous 1D multicrystalline nanowire (conf-BP@CNT) with an aspect ratio of 100, and the stabilized 1D BP with orientation priority and precise lateral dimensions can be encapsulated in CNTs. In addition, the selective spatially confined growth mechanism and nucleation kinetics of conf-BP are proposed. Due to the nanochannel support of the CNT, BP only grows inside the CNT instead of outside the wall. Owing to the unique confined interaction, efficient and stable rhodamine B (RhB) degradation performance is achieved from 1D conf-BP@CNT.

RESULTS AND DISCUSSION

In the synthetic process (Figure 1a), red phosphorus, tin, iodine, and CNTs are mixed and sealed in a vacuum quartz tube that is placed horizontally in a muffle furnace. The furnace is heated to 650 °C for 2 h, and after slow cooling to room temperature, conf-BP@CNT is obtained at the low-temperature end. The 1D conf-BP@CNT is characterized by transmission electron microscopy (TEM), and as shown in Figure S1, the 1D coaxial nanowires of conf-BP@CNT have lengths of several micrometers and diameters of about ten nanometers. The energy-dispersive X-ray spectroscopy (EDS) maps reveal similar distributions of carbon and phosphorus (Figure S2). The average aspect ratio of conf-BP@CNT is about 100, which would be difficult to accomplish by conventional mechanical liquid exfoliation or ion intercalation.[47] The aspect ratio of the BP nanowire is related to the inner diameter of the CNT template. The typical conf-BP wires with aspect ratios as large as 100 are shown in Figures S1, S5, and S17. Raman scattering can distinguish BP from other phosphorus (P) allotropes. As shown in Figure 1b, except for the D and G bands of the CNT, both conf-BP@CNT and bulk BP exhibit three characteristic bands assigned to the A_g^1, B_{2g}, and A_g^2 vibration modes. Upon excitation with the same power, the Raman intensity of BP in conf-BP@CNT is much smaller than that in bulk BP, suggesting that the outer CNT blocks some of the signals. Furthermore, electron energy loss spectroscopy (EELS) is an effective method to identify different atoms and analyze the coordination states. The carbon K-edge EELS signal at 286.5 eV (Figure 1c) arises from the outer CNT shell, and the P K-edge peak at 2100.4 eV (Figure 1d) indicates elementary P instead of phosphide or phosphate. Similar to the freestanding mechanically exfoliated BP nanosheets (Figure S3), the P $L_{2,3}$-edge and P L_1-edge peaks of conf-BP@CNT are found at 132.6 and 189.9 eV, respectively, and the core-loss peak locations are different from those of other P allotropes.[48−50] The distinctive signal distributions in the high-angle annular dark-field scanning transmission electron microscopy (HAADF-STEM) image (Figure 1e) and EELS maps (Figures 1f and S4) provide evidence about the uniformity and purity of conf-BP in the single CNT. Additionally, the absence of the P_xO_y peak in the EELS spectrum of conf-BP@CNT implies that the outer CNT protects conf-BP from the external environment, especially against oxidation. These results provide unequivocal evidence enabling determination via crystallography that conf-BP is confined within CNTs.

https://doi.org/10.1021/acsami.3c12660
ACS Appl. Mater. Interfaces 2023, 15, 54157−54165

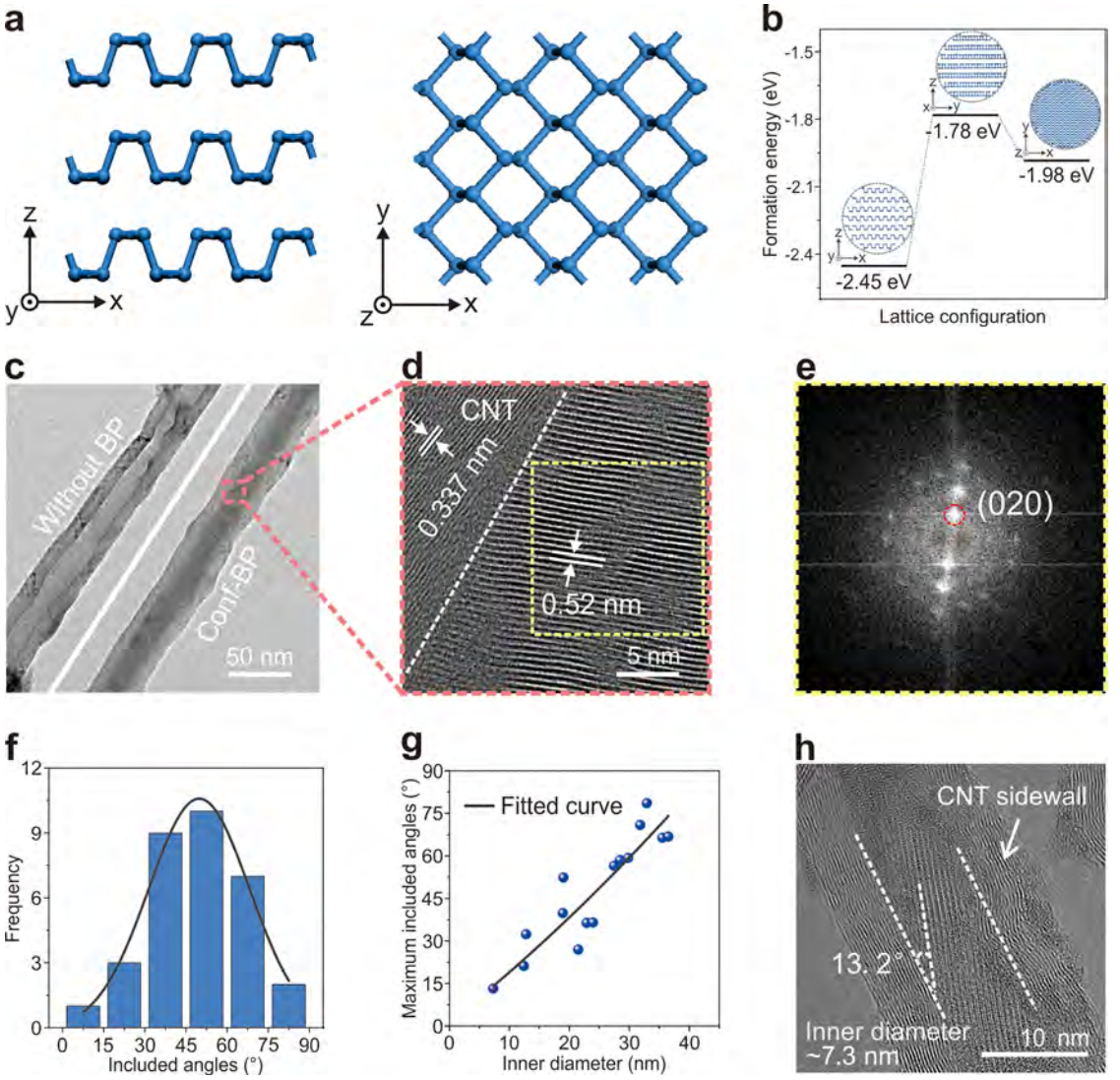

Figure 2. (a) Schematic of BP and crystal axes (*x*, *y*, *z*). (b) Simulated Gibbs energies of formation for the three different configurations of conf-BP@CNT. Left: conf-BP@CNT-*y*, middle: conf-BP@CNT-*x*, and right: conf-BP@CNT-*z*. (c) TEM images of a single blank CNT and conf-BP@CNT. (d) Lattice fringes of the area demarcated by the orange dotted line in (c). (e) The fast Fourier transform pattern of the area marked by the yellow dotted line in (d). (f) Statistical distribution of conf-BP growth at different angles. (g) Correlation between the inner diameter of the CNT and maximum conf-BP growth angles. (h) TEM images of conf-BP grown in CNTs with inner diameters of 7.3 nm.

The reproducibility of the spatial confinement growth strategy is investigated by several independent experiments (Figure S5) using CNTs with different inner diameters. As shown in Figure S6, the statistics obtained from 128 conf-BP@CNT samples demonstrate that BP can be confined in CNTs with inner diameters ranging from 7 to 37 nm, and the filling efficiency is 40−60%. Besides, we have attempted to grow BP into CNTs with fewer walls. No matter whether it is the double-walled CNT with an inner diameter of less than 1 nm or the 10-layer wall of CNT with an inner diameter of less than 4 nm, BP is rarely observed (Figure S7). In this case, the lateral dimension of conf-BP could be precisely controlled by the inner diameter size of the CNT due to the complete filling. The CNT inevitably influences the atomic arrangement of conf-BP due to the interfacial interaction; therefore, the structure of conf-BP is further studied.

The arrangement of the conf-BP lattice is an important factor that is directly related to its growth orientation and the exposed interface. *x*, *y*, and *z* are used to stipulate the BP orientation (Figure 2a), and three configurations are assessed theoretically by filling BP into the narrow CNT (diameter 4 nm) using different growth orientation models (conf-BP@CNT-*x*, conf-BP@CNT-*y*, conf-BP@CNT-*z*), as shown by the BP crystal axis parallel to the CNT inner wall (structures before relaxation in Figure S8a−c and structures after relaxation in Figure S8e−j). Among the three configurations, conf-BP@CNT-*y* shows the lowest formation energy of −2.45 eV, much less than the formation energies of conf-BP@CNT-*x* (−1.78 eV) and conf-BP@CNT-*z* (−1.98 eV, Figure 2b). However, the BP lattice in conf-BP@CNT-*y* presents the most drastic distortions among the three configurations after full relaxation (Figure S8f). The nonrational distortions suggest that conf-BP@CNT-*y* is an unstable configuration in a narrow CNT; thus, conf-BP@CNT-*z* is the most probable configuration in a narrow CNT due to its lower formation energy than that of conf-BP@CNT-*x*. Conf-BP with mixed orientations is further considered for the 6 nm wide CNT (conf-BP@CNT-mix, Figure S8d,h), and the tolerance of the

https://doi.org/10.1021/acsami.3c12660
ACS Appl. Mater. Interfaces 2023, 15, 54157−54165

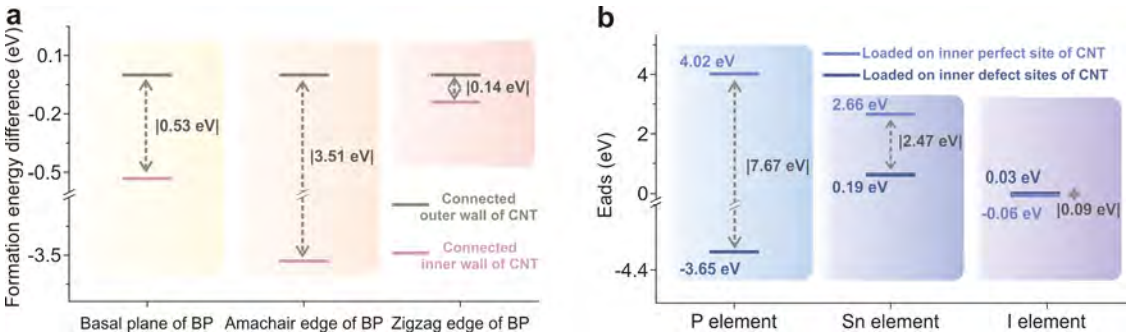

Figure 3. (a) Formation energies of the three different BP fragments loaded on the inner or outer wall (Type I, the basal plane attached to the CNT, Type II, the armchair edge connected to the CNT, and Type III, the zigzag edge connected to the CNT. (b) Energy profiles of P, Sn, and I elements incorporated with the CNT. Point defect was taken as simplified model structures of the inner wall of CNT defect.

growth orientation is higher for the wide CNT than that for the narrow CNT. These theoretical simulation results remind us that the growth orientation of conf-BP would be affected by the interaction of the CNT and depended on the inner diameter size of the CNT.

Figure 2c compares the pristine CNT and conf-BP@CNT, disclosing a bigger contrast in the central region of conf-BP@CNT indicative of the spatially confined growth of 1D BP. The high-resolution TEM (HR-TEM) image (Figure 2d) shows that the lattice fringes are related to the interlayer spacing of 0.337 nm of CNT, and the (020) spacing of 0.52 nm corresponds to BP. The fast Fourier transform pattern of the inner area corroborates the (020) facet of BP (Figure 2e). The (020) facet of conf-BP and the axial direction of the CNT would form particular angles; therefore, the growth angle defined as that between the (020) facet of conf-BP and the axial direction of the CNT is evaluated (Figures 2f–h and S9). As shown in Figure 2f, the statistical growth angle ranges from 13 to 78°. The relationship between the CNT inner diameter and the maximum angle for the CNT with a specific diameter is investigated by a linear correlation (Figure 2g), which shows that the growth orientation of conf-BP in the CNT depends on the inner diameter of the CNT. The TEM images of conf-BP grown in CNTs with different inner diameters are depicted in Figures 2h and S9. The BP atomic layer tends to grow along the axial direction of the tube in the narrow CNT (Figure 2h), but the BP orientation is more random in wider CNTs with a diameter of more than 10 nm (Figure S9). Such a configuration of conf-BP is in agreement with our results of theoretical investigation that the wide CNT inner wall does not have strong interactions with the crystal face of BP; otherwise, the orientation of conf-BP is more consistent in narrow CNTs.

In the spatially confined growth of conf-BP in CNTs, an important precondition is that the BP fragments are more thermodynamically stable on the inner wall than the outer wall of the CNT, and therefore, density functional theory (DFT) calculation is performed. In the simulation models, the BP fragments are incorporated into the CNT on three different surfaces, namely, basal planes, armchair edges, and zigzag edges. As shown in Figures 3a and S10, all of the configurations with BP fragments loaded in CNTs have lower formation energies than those loaded outside the CNTs. The results suggest that the BP fragments prefer to grow in CNTs thermodynamically. On the other hand, the nucleation kinetics also is investigated through DFT calculation. As shown in Figure 3b, the P, Sn, and I atoms are incorporated with the inner or outer walls of CNTs. Because of the anomalously stable hybrid structure of sp^2 carbon, all three atoms show similar positive adsorption energies on the perfect CNT structure. Besides the perfect sp^2 structure, diverse defects usually exist in the CNTs. The X-ray photoelectron spectroscopy (XPS) measurement of CNTs is carried out to verify the existence of defects (Figure S11). The high-resolution C 1s spectrum of CNTs shows three peaks corresponding to sp^2 C=C bonds (284.4 eV), sp^3-hybridized C−C bonds (285.0 eV), and the C−O group (288.7 eV). These results indicate the existence of functional groups and defect sites in the CNT. The defect model used in this work is a point vacancy defect constructed by a 12-carbon atomic ring (Figure S12). Compared with the outer wall point defect of the CNT, the formation energy of the inner wall point defect is much lower (about 0.4 eV), indicating a higher possibility of the formation of an inner defect on the CNT. Therefore, the inner wall point defect model is employed to reveal the defect impact on species absorption and nucleation, showing that the adsorption energy of P, Sn, and I atoms on inner defect sites is significantly lower than that of atoms loaded on the perfect structure. Hence, the unsaturated coordination defect sites tend to preferentially combine the atoms with rich valent electrons. Meanwhile, the point defect on the outer wall can also reduce the absorption energy of atoms (Figure S13), which suggests that the defect sites of the CNT would enhance the absorption of the evaporated species on the CNT surface kinetically and further assist in nucleation. Considering the experimental phenomena of the selectively confined growth in CNTs, the whole selective growth reaction is dominantly controlled by the thermodynamical process. The defect has assisted the initial absorption step. Moreover, similar to previous reports, the nanochannel of CNTs offers a capillarity force and enables a strong space restriction.[51−53] When the as-prepared conf-BP@CNT is treated at a high temperature of 700 °C, the phosphorus wires are still filled in CNTs despite the destroyed lattice (Figure S14). Therefore, the capillarity force and the spatial confinement are regarded as important factors for selective growth.

Furthermore, to systemically investigate the selectively confined nucleation process of 1D BP into the CNT, the CVT reaction was carried out, and the samples were cooled at different temperatures rapidly to investigate the intermediate products. Benefiting from the spatial confinement effect of the CNT, the different intermediate stages can be captured under rapid quenching. In the initial heating stage, red phosphorus and iodine are converted into gas, and the tin reacts with the

https://doi.org/10.1021/acsami.3c12660
ACS Appl. Mater. Interfaces 2023, 15, 54157−54165

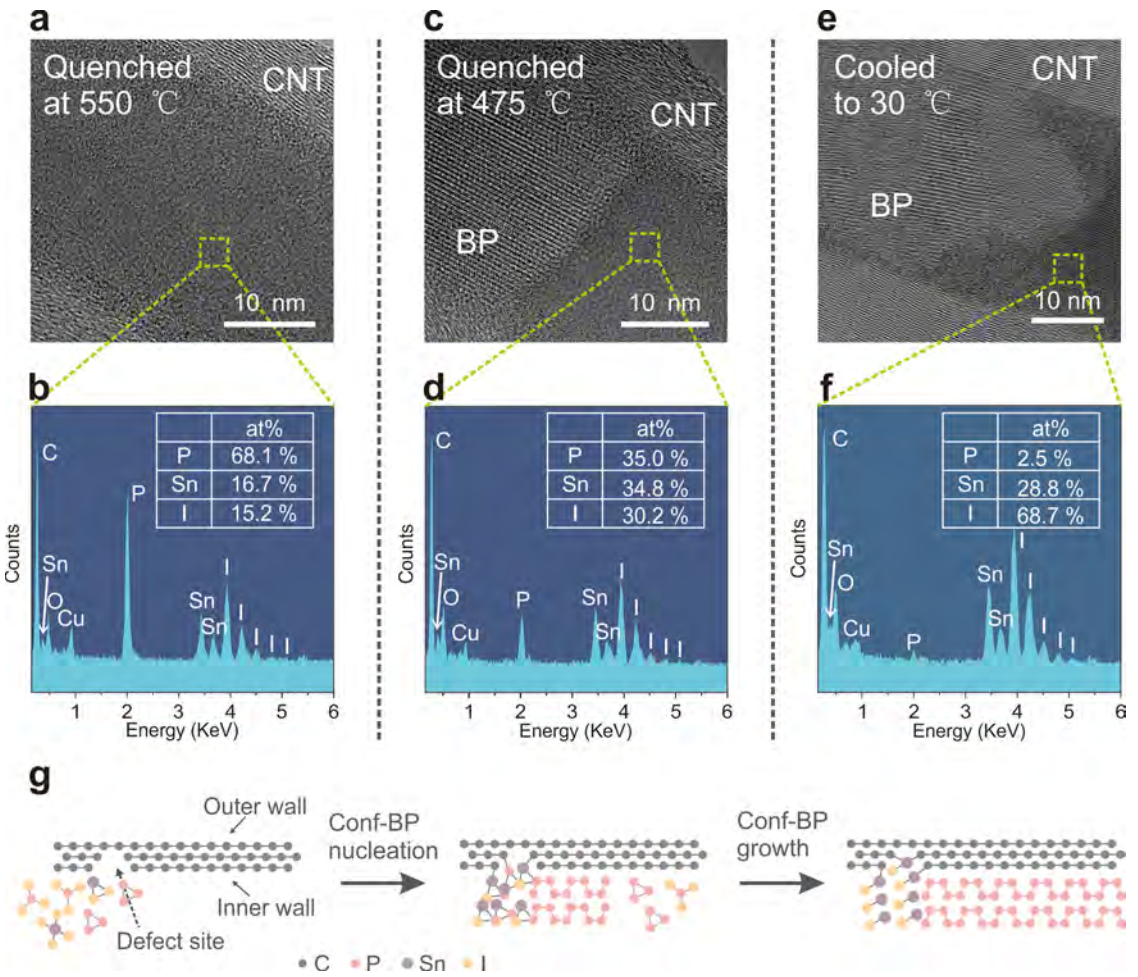

Figure 4. Spatial confinement process of the BP wire within the CNT. (a) TEM image of the CNT containing the amorphous filling in the early growth stage. (b) EDS spectrum of the inner area in (a). (c) TEM image of conf-BP@CNT for the intermediate state. (d) EDS spectrum of the marked area in (c). (e) TEM image of the nucleation interface of conf-BP. (f) EDS spectrum of the marked area in (e). (g) Schematic diagram showing the growth of conf-BP@CNT.

phosphorus and iodine vapor. After long-time transport, the vapor would diffuse into the CNT. When the reaction is quenched in the early growth stage at 550 °C (the product is named quenched *sample I*), the CNT terminal is filled with amorphous materials, which are identified by EDS to be the Sn−I−P compound (Figure 4a). The atomic concentrations of Sn, I, and P are 16.7, 15.2, and 68.1%, respectively (Figure 4b). If the reaction is quenched at 475 °C (the product is named quenched *sample II*), then the CNT is filled with both crystalline and amorphous materials (Figure 4c). Apart from crystalline BP with clear lattice fringes, the amorphous components consist of Sn, I, and P (Figure 4d). It should be noted that the atomic concentrations of quenched *sample II* are different from those of quenched *sample I*. P content changes from 68.1 to 35.0%, demonstrating that the prefilled amorphous high phosphorus-containing Sn−I−$P_{(0.68)}$ in the CNT has decomposed into low-phosphorus-containing amorphous Sn−I−$P_{(0.35)}$ and crystalline BP. When growth is completed, the nucleation interface transforms completely into the two crystalline phases (Figure 4e). The lattice fringes in the STEM image and elemental distributions obtained by EDS (Figure 4f) show that the product consists of BP and Sn−I compounds. Both the line scan (Figure S15) and the area elemental distribution (Figure S16) agree with the EDS spectrum and further demonstrate the nucleation interface and two different phases. The wide area TEM images (Figure S17) show that Sn−I compounds and the longer conf-BP nanowires are randomly distributed throughout the CNTs. The results demonstrate that as soon as the raw vapor has sufficiently diffused and absorbed in the CNT, the nucleation of BP in the CNT is mainly impacted by the temperature-controlled phase separation and element redistribution.

Based on the aforementioned results, a spatially confined growth mechanism is proposed, as shown in Figure 4g. As the sealed bottle is heated to a temperature (higher than 550 °C) that exceeds the boiling point of red phosphorus and iodine, it is vaporized to fill the inner space of the CNT. Meanwhile, tin reacts with iodine to form gaseous SnI_4 and SnI_2, which flow into the CNT with P gas and P−I gas. Because the inner wall defects have a better absorption ability of the vapor species than the perfect carbon structure, the concentrations of Sn, I, and P are higher in the CNT than on the outside. Therefore, the amorphous Sn−I−P bond is observed in quenched *sample I*. As the result of the combination of temperature decline and the enriched phosphorus in raw materials, the Sn−I−P compound decomposes and reacts with gaseous P to generate conf-BP. Since the BP fragments have lower formation energies on the inner wall of the CNT than the outer wall, growth takes

https://doi.org/10.1021/acsami.3c12660
ACS Appl. Mater. Interfaces 2023, 15, 54157−54165

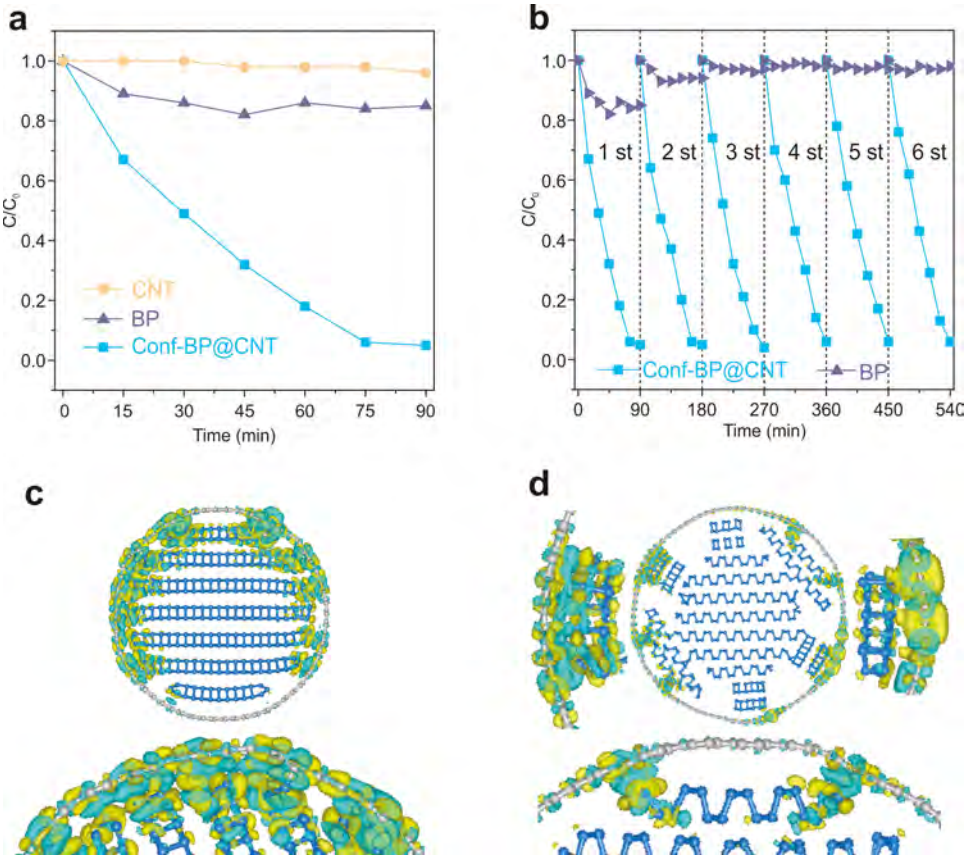

Figure 5. (a) Photocatalytic characteristics of conf-BP@CNT, BP, and CNT in RhB degradation. (b) Cycling stability of conf-BP@CNT and BP in the RhB degradation experiment. (c, d) The charge difference distribution of conf-BP@CNT-*x* (c) and conf-BP@CNT-*mix* (d), where the charge accumulation in the interface was represented by yellow and green isosurfaces, respectively.

place mainly inside the CNT, and the prefilled P in the CNT is finally converted into a 1D BP wire.

The contact between different materials can alter the interfacial charge transfer and material hybridization properties. RhB degradation experiments are performed to investigate the photocatalytic performance of the 1D core−shell conf-BP@CNT nanowires. As shown in Figure S18, the absorption peak of RhB at 554 nm decreases gradually as the irradiation time prolongs. The RhB-maintained concentration ratios in Figure 5a demonstrate that conf-BP@CNT delivers much better photocatalytic performance than bare BP and CNT. RhB is completely decomposed by conf-BP@CNT in 75 min, while only 20% of RhB is decomposed by bare BP. The photocatalysis of individual BP is limited by the fast electron−hole recombination after incident light absorption, leading to ineffective photocatalytic activity. Besides, the increase of oxidation risk in an aqueous environment is attributed to the unpaired lone electrons of BP, resulting in the photocatalytic activity failure of BP. Using CNTs as the protection layer to avoid direct contact with the surroundings is an effective method to stabilize BP. The repeatabilities of samples are further determined by repeating the degradation experiments six times (Figure 5b). The photocatalytic performance of conf-BP@CNT is similar in the six trials. However, the photocatalytic performance of bare BP declines rapidly, indicating better stability than BP.

As shown in the charge density patterns (Figure 5c,d), when 1D BP is confined in the CNT, charges are depleted on conf-BP and accumulate on the inner wall of the CNT regardless of the BP arrangement in the CNT. In particular, if the edges of BP contact the inner wall of the CNT with a diameter of 4 nm (Figure 5c), charge redistribution occurs between the edge dangling bonds of BP and the CNT. If BP is in contact with the CNT with an inner wall diameter of 6 nm (Figure 5d), charges are evenly redistributed between the two adjacent surfaces. Considering that the phosphorus atomic coordination number of the edge dangling bond is smaller than that of the basal plane, it is supposed that charge transfer arises mainly from the unpaired lone electrons of BP, and consequently, interfacial electron localization would reduce the electron−hole pair coupling risk of BP. More importantly, the conducting CNT acts as the electron acceptor to inhibit charge recombination of the photogenerated carriers in BP and transfer charge to dye molecules. Moreover, the inner wall defect can accelerate the charge transfer between BP and the CNT, and the outer wall defects would act as catalysis sites. Attributing to the above interface interactions in conf-BP@CNT, the photocatalytic efficiency and stability of BP are greatly improved.

CONCLUSIONS

In conclusion, 1D BP nanowires are synthesized by a spatially confined strategy; simultaneously, the precise nanoscale control over the lateral dimensions of conf-BP is achieved by the inner diameter of CNTs. The aspect ratio of the conf-BP wire is about 100. Confinement within different-inner-diameter CNTs defines the orientation arrangement of conf-BP. Notably, capillarity and the thermodynamic priority caused

https://doi.org/10.1021/acsami.3c12660
ACS Appl. Mater. Interfaces 2023, 15, 54157−54165

by the nanochannel of CNTs have dominated the selective spatially confined growth of BP. Moreover, benefiting from the capsule-like effect of CNTs, intermediates and the possible underlying growth mechanism of the BP wire are revealed. Because of efficient charge separation on conf-BP@CNT and protection by the CNT shell, the photocatalytic activity and stability properties are observed from the conf-BP@CNT boding well for the application of 1D confined BP to nanocatalysis. The results reveal a novel spatial confinement strategy and have great potential to extend to produce other types of low-dimension nanoconfined structures.

EXPERIMENTAL SECTION

Synthesis of conf-BP@CNT. conf-BP was prepared by CVT. Commercial CNTs (Timesnano) were degassed for 8 h, and then red phosphorus (Western Elements, 99.999%), tin particles (Aldrich, 99.9%), and iodine (Aldrich, 99.99%) were put into a quartz tube. The degassed commercial CNTs were placed in the quartz tube and separated from the raw materials by silica wool. The quartz tube was evacuated and sealed. Because of the silica wool separation, the CNTs and raw materials were at the two ends of the tube. The sealed quartz tube was then placed in a muffle furnace horizontally with the raw materials close to the heating wire, while the CNTs were close to the furnace door. The temperature was raised from room temperature to 650 °C, and after keeping at 650 °C for 120 min, the temperature was slowly reduced to 380 °C in 1200 min. Finally, the product was cooled slowly to room temperature for 240 min, and the sealed quartz tube was transferred to a glovebox to take out the conf-BP@CNT powder.

Preparation of Bare BP Nanosheets. The liquid-exfoliated BP nanosheets were analyzed by EELS. In brief, the bulk BP (15 mg) was ground with ethanol (20 mL) with an agate mortar for 30 min; 30 mL of ethanol was added and sonicated in a water bath at 40 kHz for 36 h, and the BP nanosheets were laid on a copper mesh to conduct EELS.

Reaction Interruption Experiments. Owing to the capsule-like effect of CNTs, the intermediate state of conf-BP could be displayed on the nanoscale via TEM measurement. Therefore, a series of controlled interrupt experiments were conducted to investigate the process of nucleation and growth of conf-BP. To avoid a continuous reaction between the intermediate product and the gaseous substance, the high-temperature end of the ampule was rapidly cooled so that the gaseous compound in the ampule was rapidly condensed in this area. In the first stage, the reactants were heated to 650 °C; meanwhile, the gaseous compounds were produced. Following, the gaseous compounds flowed into the CNT and generated the CNT containing high-temperature products as the temperature declined. Then, the nucleation process of conf-BP occurred at a lower temperature. In the end, the final product of conf-BP was obtained at room temperature. Thus, at the specified temperature, we interrupted the reaction to measure these intermediate states. To avoid contamination, the CNT containing intermediate products was taken out from a glovebox full of nitrogen.

Photocatalytic Experiments on RhB Degradation. 3.0 mg of the photocatalyst was suspended in 12 mL of the RhB aqueous solution (5.0 mg·L^{-1}). The suspension was stirred in the dark for 30 min to achieve the adsorption−desorption equilibrium of RhB before light-emitting diode (LED) irradiation. Utilizing flowing water, the temperature of the photocatalytic system was kept at room temperature. The amount of RhB was determined by UV−vis spectrophotometry (Hitachi U-3900) and Lambert−Bill law. Besides, based on the decreased amount of RhB, the photocatalytic performance of the samples was calculated.

Material Characterization. The TEM images, high-resolution TEM images, HAADF images, and EDS spectra were acquired on a Tecnai G2 F20 S-Twin at an acceleration voltage of 300 kV. The aberration-corrected TEM (AC-TEM) images, HAADF-STEM image, and EELS spectra were obtained on an FEI Themis G2 at 60 kV. Raman scattering was carried out on a Jobin Yvon Horiba HR (France) confocal Raman microscope with a 633 nm laser. XPS was performed with a Thermo Fisher Escalab 250Xi instrument using monochromatic Al kg radiation.

DFT Calculation. An armchair CNT (30, 30) with a diameter of ∼4 nm and an armchair CNT (45, 45) with a diameter of ∼6 nm were used in the model. The periodic boundary conditions were along the tube axis. DFT simulations were carried out using the freely available CP2K/Quickstep package and density functional theory (DFT) based on the hybrid Gaussian plane wave (GPW) scheme36.[41] The 2s and 2p electrons of C and P were treated as valence electrons, and the rest of the core electrons were represented by Goedecker−Teter−Hutter (GTH) pseudopotentials.[42,43] The Perdew−Burke−Ernzerhof (PBE) functional[44] with Grimme's dispersion correction was employed.[45] The Gaussian basic sets were double-ζ with one set of polarization functions (DZVP),[46] and the plane wave cutoff for the electron density was 400 Ry. In the static calculation, the geometry was optimized by the Broyden−Fletcher−Goldfarb−Shanno (BFGS) minimizer. Because of the large size of the supercells, only the Γ-point was used in the calculation.

ASSOCIATED CONTENT

Supporting Information

The Supporting Information is available free of charge at https://pubs.acs.org/doi/10.1021/acsami.3c12660.

More TEM images; EDS, XPS, and DFT calculation results; and Figures S1−S18 (PDF)

AUTHOR INFORMATION

Corresponding Author

Jiahong Wang − *Shenzhen Institute of Advanced Technology, Chinese Academy of Sciences, Shenzhen 518055, P. R. China; University of Chinese Academy of Sciences, Beijing 100049, P. R. China; Department of Physics, Department of Materials Science and Engineering, and Department of Biomedical Engineering, City University of Hong Kong, Hong Kong, P. R. China;* orcid.org/0000-0002-6743-7923; Email: jh.wang1@siat.ac.cn

Authors

Yumin Da − *Shenzhen Institute of Advanced Technology, Chinese Academy of Sciences, Shenzhen 518055, P. R. China; University of Chinese Academy of Sciences, Beijing 100049, P. R. China*

Xue Zhang − *Shenzhen Institute of Advanced Technology, Chinese Academy of Sciences, Shenzhen 518055, P. R. China; University of Chinese Academy of Sciences, Beijing 100049, P. R. China*

Chao Peng − *Shenzhen Institute of Advanced Technology, Chinese Academy of Sciences, Shenzhen 518055, P. R. China; University of Chinese Academy of Sciences, Beijing 100049, P. R. China*

Hao Huang − *Shenzhen Institute of Advanced Technology, Chinese Academy of Sciences, Shenzhen 518055, P. R. China;* orcid.org/0000-0001-9785-996X

Shuai Zhang − *Shenzhen Institute of Advanced Technology, Chinese Academy of Sciences, Shenzhen 518055, P. R. China;* orcid.org/0000-0003-3535-1233

Paul K. Chu − *Department of Physics, Department of Materials Science and Engineering, and Department of Biomedical Engineering, City University of Hong Kong, Hong Kong, P. R. China;* orcid.org/0000-0002-5581-4883

Xue-Feng Yu − *Shenzhen Institute of Advanced Technology, Chinese Academy of Sciences, Shenzhen 518055, P. R. China;*

https://doi.org/10.1021/acsami.3c12660
ACS Appl. Mater. Interfaces 2023, 15, 54157−54165

University of Chinese Academy of Sciences, Beijing 100049, P. R. China; Biomedical Imaging Science and System Key Laboratory, Chinese Academy of Sciences, Shenzhen 518055, P. R. China; orcid.org/0000-0003-2566-6194

Complete contact information is available at: https://pubs.acs.org/10.1021/acsami.3c12660

Author Contributions

[⊥]Y.D., X.Z., and C.P. contributed equally to this work. All authors have given approval to the final version of the manuscript.

Notes

The authors declare no competing financial interest.

■ ACKNOWLEDGMENTS

The authors acknowledge the financial support from the National Natural Science Foundation of China (21975280 and 22379159), Youth Innovation Promotion Association Chinese Academy of Sciences (2020354), Natural Science Foundation of Guangdong Province (2022A1515010076 and 2023A1515030178), Shenzhen Science and Technology Program (JCYJ20220818100806014), and City University of Hong Kong Strategic Research Grant (SRG) No. 7005505.

■ ABBREVIATIONS

BP, black phosphorus; CNT, carbon nanotube; conf-BP@CNT, confining BP into carbon nanotube; 2D, two-dimensional; 1D, one-dimensional; MoS_2, molybdenum sulfide; TMDs, transition metal dichalcogenides; BN, boron nitride; CVT, chemical vapor-phase transport; conf-BP, confine 2D BP; RhB, rhodamine B; AC-TEM, aberration-corrected transmission electron microscopy; EDS, energy-dispersive X-ray spectroscopy; EELS, electron energy loss spectroscopy; HAADF-STEM, high-angle annular dark-field scanning transmission electron microscopy; GPW, Gaussian plane wave; DFT, density functional theory; XPS, X-ray photoelectron spectroscopy; GTH, Goedecker−Teter−Hutter; PBE, Perdew−Burke−Ernzerhof; BFGS, Broyden−Fletcher−Goldfarb−Shanno

■ REFERENCES

(1) Wang, C.; He, Q.; Halim, U.; Liu, Y.; Zhu, E.; Lin, Z.; Xiao, H.; Duan, X.; Feng, Z.; Cheng, R.; Weiss, N. O.; Ye, G.; Huang, Y. C.; Wu, H.; Cheng, H. C.; Shakir, I.; Liao, L.; Chen, X.; Goddard, W. A.; Huang, Y.; Duan, X. Monolayer Atomic Crystal Molecular Superlattices. *Nature* **2018**, *555*, 231−236.

(2) Liu, Y. T.; Li, D.; Yu, J.; Ding, B. Stable Confinement of Black Phosphorus Quantum Dots on Black Tin Oxide Nanotubes: A Robust, Double-Active Electrocatalyst toward Efficient Nitrogen Fixation. *Angew. Chem., Int. Ed.* **2019**, *58*, 16439−16444.

(3) Pang, X.; He, Y.; Jung, J.; Lin, Z. 1D Nanocrystals with Precisely Controlled Dimensions, Compositions, and Architectures. *Science* **2016**, *353*, 1268−1272.

(4) Ma, W.; Alonso-González, P.; Li, S.; Nikitin, A. Y.; Yuan, J.; Martín-Sánchez, J.; Taboada-Gutiérrez, J.; Amenabar, I.; Li, P.; Vélez, S.; Tollan, C.; Dai, Z.; Zhang, Y.; Sriram, S.; Kalantar-Zadeh, K.; Lee, S. T.; Hillenbrand, R.; Bao, Q. In-Plane Anisotropic and Ultra-Low-Loss Polaritons in a Natural van Der Waals Crystal. *Nature* **2018**, *562*, 557−562.

(5) Qi, P.; Luo, Y.; Shi, B.; Li, W.; Liu, D.; Zheng, L.; Liu, Z.; Hou, Y.; Fang, Z. Phonon Scattering and Exciton Localization : Molding Exciton Flux in Two Dimensional Disorder Energy Landscape. *eLight* **2021**, *1*, No. 6.

(6) Lee, D.; So, S.; Hu, G.; Kim, M.; Badloe, T.; Cho, H.; Kim, J.; et al. Hyperbolic Metamaterials : Fusing Artificial Structures to Natural 2D Materials. *eLight* **2022**, *2*, No. 1.

(7) Novoselov, K. S.; Geim, A. K.; Morozov, S. V.; Jiang, D.; Zhang, Y.; Dubonos, S. V.; Grigorieva, I. V.; Firsov, A. A. Electric Field Effect in Atomically Thin Carbon Films. *Nature* **2016**, *306*, 666−669.

(8) Chen, S.; Kim, S.; Chen, W.; Yuan, J.; Bashir, R.; Lou, J.; Van Der Zande, A. M.; King, W. P. Monolayer MoS_2 Nanoribbon Transistors Fabricated by Scanning Probe Lithography. *Nano Lett.* **2019**, *19*, 2092−2098.

(9) Luo, Y.; Tang, L.; Khan, U.; Yu, Q.; Cheng, H. M.; Zou, X.; Liu, B. Morphology and Surface Chemistry Engineering toward PH-Universal Catalysts for Hydrogen Evolution at High Current Density. *Nat. Commun.* **2019**, *10*, No. 269.

(10) Da, Y.; Liu, J.; Zhou, L.; Zhu, X.; Chen, X.; Fu, L. Engineering 2D Architectures toward High-Performance Micro-Supercapacitors. *Adv. Mater.* **2019**, *31*, No. 1802793.

(11) Guo, Z.; Zeng, Y.; Meng, F.; Qu, H.; Zhang, S.; Hu, S.; Fan, S.; Zeng, H.; Cao, R.; Prasad, P. N.; Fan, D.; Zhang, H. In - Situ Neutron - Transmutation for Substitutional Doping in 2D Layered Indium Selenide Based Phototransistor. *eLight* **2022**, *2*, No. 9.

(12) Zhang, Y. J.; Ideue, T.; Onga, M.; Qin, F.; Suzuki, R.; Zak, A.; Tenne, R.; Smet, J. H.; Iwasa, Y. Enhanced Intrinsic Photovoltaic Effect in Tungsten Disulfide Nanotubes. *Nature* **2019**, *570*, 349−353.

(13) Han, Y.; Li, M. Y.; Jung, G. S.; Marsalis, M. A.; Qin, Z.; Buehler, M. J.; Li, L. J.; Muller, D. A. Sub-Nanometre Channels Embedded in Two-Dimensional Materials. *Nat. Mater.* **2018**, *17*, 129−133.

(14) Mocking, T. F.; Bampoulis, P.; Oncel, N.; Poelsema, B.; Zandvliet, H. J. W. Electronically Stabilized Nanowire Growth. *Nat. Commun.* **2013**, *4*, No. 2387.

(15) Chang, C. H.; Ortix, C. Theoretical Prediction of a Giant Anisotropic Magnetoresistance in Carbon Nanoscrolls. *Nano Lett.* **2017**, *17*, 3076−3080.

(16) Sinha, S. S.; Sreedhara, M. B.; Tenne, R. Why Do Nanocrystals of 2D Materials Form Nanotubes and Why Is That Important? *Nano Today* **2021**, *37*, No. 101060.

(17) Calvaresi, M.; Zerbetto, F. Atomistic Molecular Dynamics Simulations Reveal Insights into Adsorption, Packing, and Fluxes of Molecules with Carbon Nanotubes. *J. Mater. Chem. A* **2014**, *2*, 12123−12135.

(18) Cui, X.; Kong, Z.; Gao, E.; Huang, D.; Hao, Y.; Shen, H.; Di, C. A.; Xu, Z.; Zheng, J.; Zhu, D. Rolling up Transition Metal Dichalcogenide Nanoscrolls via One Drop of Ethanol. *Nat. Commun.* **2018**, *9*, No. 1301.

(19) Zhao, B.; Wan, Z.; Liu, Y.; Xu, J.; Yang, X.; Shen, D.; Zhang, Z.; Guo, C.; Qian, Q.; Li, J.; Wu, R.; Lin, Z.; Yan, X.; Li, B.; Zhang, Z.; Ma, H.; Li, B.; Chen, X.; Qiao, Y.; Shakir, I.; Almutairi, Z.; Wei, F.; Zhang, Y.; Pan, X.; Huang, Y.; Ping, Y.; Duan, X.; Duan, X. High-Order Superlattices by Rolling up van Der Waals Heterostructures. *Nature* **2021**, *591*, 385−390.

(20) Xiang, R.; Inoue, T.; Zheng, Y.; Kumamoto, A.; Qian, Y.; Sato, Y.; Liu, M.; Tang, D.; Gokhale, D.; Guo, J.; Hisama, K.; Yotsumoto, S.; Ogamoto, T.; Arai, H.; Kobayashi, Y.; Zhang, H.; Hou, B.; Anisimov, A.; Maruyama, M.; Miyata, Y.; Okada, S.; Chiashi, S.; Li, Y.; Kong, J.; Kauppinen, E. I.; Ikuhara, Y.; Suenaga, K.; Maruyama, S. One-Dimensional van Der Waals Heterostructures. *Science.* **2020**, *367*, 537−542.

(21) Liao, M.; Wei, Z.; Du, L.; Wang, Q.; Tang, J.; Yu, H.; Wu, F.; Zhao, J.; Xu, X.; Han, B.; Liu, K.; Gao, P.; Polcar, T.; Sun, Z.; Shi, D.; Yang, R.; Zhang, G. Precise Control of the Interlayer Twist Angle in Large Scale MoS_2 Homostructures. *Nat. Commun.* **2020**, *11*, No. 2153.

(22) Wang, L.; Xu, X.; Zhang, L.; Qiao, R.; Wu, M.; Wang, Z.; Zhang, S.; Liang, J.; Zhang, Z.; Zhang, Z.; Chen, W.; Xie, X.; Zong, J.; Shan, Y.; Guo, Y.; Willinger, M.; Wu, H.; Li, Q.; Wang, W.; Gao, P.; Wu, S.; Zhang, Y.; Jiang, Y.; Yu, D.; Wang, E.; Bai, X.; Wang, Z. J.; Ding, F.; Liu, K. Epitaxial Growth of a 100-Square-Centimetre Single-

Crystal Hexagonal Boron Nitride Monolayer on Copper. *Nature* **2019**, *570*, 91−95.
(23) Zhang, J.; Zhao, D.; Xiao, D.; Ma, C.; Du, H.; Li, X.; Zhang, L.; Huang, J.; Huang, H.; Jia, C. L.; Tománek, D.; Niu, C. Assembly of Ring-Shaped Phosphorus within Carbon Nanotube Nanoreactors. *Angew. Chem., Int. Ed.* **2017**, *56*, 1850−1854.
(24) Wu, Y.; Cheng, G.; Katsov, K.; Sides, S. W.; Wang, J.; Tang, J.; Fredrickson, G. H.; Moskovits, M.; Stucky, G. D. Composite Mesostructures by Nano-Confinement. *Nat. Mater.* **2004**, *3*, 816−822.
(25) Hart, M.; Chen, J.; Michaelides, A.; Sella, A.; Shaffer, M. S. P.; Salzmann, C. G. One-Dimensional Arsenic Allotropes: Polymerization of Yellow Arsenic Inside Single-Wall Carbon Nanotubes. *Angew. Chem., Int. Ed.* **2018**, *57*, 11649−11653.
(26) Meyer, R. R.; Sloan, J.; Dunin-Borkowski, R. E.; Kirkland, A. I.; Novotny, M. C.; Bailey, S. R.; Hutchison, J. L.; Green, M. L. H. Discrete Atom Imaging of One-Dimensional Crystals Formed within Single-Walled Carbon Nanotubes. *Science* **2000**, *289*, 1324−1326.
(27) Warner, J. H.; Plant, S. R.; Young, N. P.; Porfyrakis, K.; Kirkland, A. I.; Briggs, G. A. D. Atomic Scale Growth Dynamics of Nanocrystals within Carbon Nanotubes. *ACS Nano* **2011**, *5*, 1410−1417.
(28) Slade, C. A.; Sanchez, A. M.; Sloan, J. Unprecedented New Crystalline Forms of SnSe in Narrow to Medium Diameter Carbon Nanotubes. *Nano Lett.* **2019**, *19*, 2979−2984.
(29) Chen, W.; Fan, Z.; Zhang, B.; Ma, G.; Takanabe, K.; Zhang, X.; Lai, Z. Enhanced Visible-Light Activity of Titania via Confinement inside Carbon Nanotubes. *J. Am. Chem. Soc.* **2011**, *133*, 14896−14899.
(30) Li, X.; Zhang, J.; Wang, R.; Huang, H.; Xie, C.; Li, Z.; Li, J.; Niu, C. In Situ Synthesis of Carbon Nanotube Hybrids with Alternate MoC and MoS_2 to Enhance the Electrochemical Activities of MoS_2. *Nano Lett.* **2015**, *15*, 5268−5272.
(31) Tang, L.; Meng, X.; Deng, D.; Bao, X. Confinement Catalysis with 2D Materials for Energy Conversion. *Adv. Mater.* **2019**, *31*, No. 1901996.
(32) Tian, H.; Wang, J.; Lai, G.; Dou, Y.; Gao, J.; Duan, Z.; Feng, X.; Wu, Q.; He, X.; Yao, L.; Zeng, L.; Liu, Y.; Yang, X.; Zhao, J.; Zhuang, S.; Shi, J.; Qu, G.; Yu, X. F.; Chu, P. K.; Jiang, G. Renaissance of Elemental Phosphorus Materials: Properties, Synthesis, and Applications in Sustainable Energy and Environment. *Chem. Soc. Rev.* **2023**, *52*, 5388−5484.
(33) Zeng, L.; Zhang, X.; Liu, Y.; Yang, X.; Wang, J.; Liu, Q.; Luo, Q.; Jing, C.; Yu, X. F.; Qu, G.; Chu, P. K.; Jiang, G. Surface and Interface Control of Black Phosphorus. *Chem* **2022**, *8*, 632−662.
(34) Wang, Z. J.; Dong, J.; Cui, Y.; Eres, G.; Timpe, O.; Fu, Q.; Ding, F.; Schloegl, R.; Willinger, M. G. Stacking Sequence and Interlayer Coupling in Few-Layer Graphene Revealed by in Situ Imaging. *Nat. Commun.* **2016**, *7*, No. 13256.
(35) Peng, L.; Yuan, Y.; Li, G.; Yang, X.; Xian, J. J.; Yi, C. J.; Shi, Y. G.; Fu, Y. S. Observation of Topological States Residing at Step Edges of WTe2. *Nat. Commun.* **2017**, *8*, No. 659.
(36) Guimarães, M. H. D.; Gao, H.; Han, Y.; Kang, K.; Xie, S.; Kim, C. J.; Muller, D. A.; Ralph, D. C.; Park, J. Atomically Thin Ohmic Edge Contacts between Two-Dimensional Materials. *ACS Nano* **2016**, *10*, 6392−6399.
(37) Favron, A.; Gaufrès, E.; Fossard, F.; Phaneuf-Laheureux, A. L.; Tang, N. Y. W.; Lévesque, P. L.; Loiseau, A.; Leonelli, R.; Francoeur, S.; Martel, R. Photooxidation and Quantum Confinement Effects in Exfoliated Black Phosphorus. *Nat. Mater.* **2015**, *14*, 826−832.
(38) Hart, M.; White, E. R.; Chen, J.; McGilvery, C. M.; Pickard, C. J.; Michaelides, A.; Sella, A.; Shaffer, M. S. P.; Salzmann, C. G. Encapsulation and Polymerization of White Phosphorus Inside Single-Wall Carbon Nanotubes. *Angew. Chem., Int. Ed.* **2017**, *56*, 8144−8148.
(39) Zhang, J.; Fu, C.; Song, S.; Du, H.; Zhao, D.; Huang, H.; Zhang, L.; Guan, J.; Zhang, Y.; Zhao, X.; Ma, C.; Jia, C. L.; Tománek, D. Changing the Phosphorus Allotrope from a Square Columnar Structure to a Planar Zigzag Nanoribbon by Increasing the Diameter of Carbon Nanotube Nanoreactors. *Nano Lett.* **2020**, *20*, 1280−1285.
(40) Li, J.; Jin, H.; Yuan, Y.; Lu, H.; Su, C.; Fan, D.; Li, Y.; Wang, J.; Lu, J.; Wang, S. Encapsulating Phosphorus inside Carbon Nanotubes via a Solution Approach for Advanced Lithium Ion Host. *Nano Energy* **2019**, *58*, 23−29.
(41) Vandevondele, J.; Krack, M.; Mohamed, F.; Parrinello, M.; Chassaing, T.; Hutter, J. Quickstep: Fast and Accurate Density Functional Calculations Using a Mixed Gaussian and Plane Waves Approach. *Comput. Phys. Commun.* **2005**, *167*, 103−128.
(42) Goedecker, S.; Teter, M.; Hutter, J. Separable Dual-Space Gaussian Pseudopotentials. *Phys. Rev. B: Condens. Matter Mater. Phys.* **1996**, *54*, 1703−1710.
(43) Hartwigsen, C.; Goedecker, S.; Hutter, J. Relativistic separable dual-space Gaussian pseudopotentials from H to Rn. *Phys. Rev. B* **1998**, *58*, 3641−3662.
(44) Perdew, J. P.; Burke, K.; Ernzerhof, M. Generalized Gradient Approximation Made Simple. *Phys. Rev. Lett.* **1996**, *77*, 3865−3868.
(45) Grimme, S.; Antony, J.; Ehrlich, S.; Krieg, H. A Consistent and Accurate Ab Initio Parametrization of Density Functional Dispersion Correction (DFT-D) for the 94 Elements H-Pu. *J. Chem. Phys.* **2010**, *132*, No. 154104.
(46) VandeVondele, J.; Hutter, J. Gaussian Basis Sets for Accurate Calculations on Molecular Systems in Gas and Condensed Phases. *J. Chem. Phys.* **2007**, *127*, No. 114105.
(47) Bat-Erdene, M.; Batmunkh, M.; Shearer, C. J.; Tawfik, S. A.; Ford, M. J.; Yu, L.; Sibley, A. J.; Slattery, A. D.; Quinton, J. S.; Gibson, C. T.; Shapter, J. G. Efficient and Fast Synthesis of Few-Layer Black Phosphorus via Microwave-Assisted Liquid-Phase Exfoliation. *Small Methods* **2017**, *1*, No. 1700260.
(48) Naclerio, A. E.; Zakharov, D. N.; Kumar, J.; Rogers, B.; Pint, C. L.; Shrivastava, M.; Kidambi, P. R. Visualizing Oxidation Mechanisms in Few-Layered Black Phosphorus via in Situ Transmission Electron Microscopy. *ACS Appl. Mater. Interfaces* **2020**, *12*, 15844−15854.
(49) Yasaei, P.; Kumar, B.; Foroozan, T.; Wang, C.; Asadi, M.; Tuschel, D.; Indacochea, J. E.; Klie, R. F.; Salehi-Khojin, A. High-Quality Black Phosphorus Atomic Layers by Liquid-Phase Exfoliation. *Adv. Mater.* **2015**, *27*, 1887−1892.
(50) Xu, F.; Ge, B.; Chen, J.; Nathan, A.; Xin, L. L.; Ma, H.; Min, H.; Zhu, C.; Xia, W.; Li, Z.; Li, S.; Yu, K.; Wu, L.; Cui, Y.; Sun, L.; Zhu, Y. Scalable Shear-Exfoliation of High-Quality Phosphorene Nanoflakes with Reliable Electrochemical Cycleability in Nano Batteries. *2D Mater.* **2016**, *3*, No. 025005.
(51) Dujardin, E.; Ebbesen, T. W.; Hiura, H.; Tanigaki, K. Capillarity and Wetting of Carbon Nanotubes. *Science* **1994**, *265*, 1850−1852.
(52) Ugarte, D.; Chatelain, A.; Heer, W. A. de. Nanocapillarity and Chemistry in Carbon Nanotubes. *Science* **1996**, *274*, 1897−1899.
(53) Chen, J. Y.; Kutana, A.; Collier, C. P.; Giapis, K. P. Electrowetting in Carbon Nanotubes. *Science* **2005**, *310*, 1480−1483.

https://doi.org/10.1021/acsami.3c12660
ACS Appl. Mater. Interfaces 2023, 15, 54157−54165

Supporting Information

Selectively confined black phosphorus nanowire in carbon nanotube

Yumin Da [a, b, ‡], *Xue Zhang* [a, b, ‡], *Chao Peng* [a, b, ‡], *Hao Huang* [a], *Shuai Zhang* [a], *Paul K. Chu* [c], *Xue-Feng Yu* [a, b, d], *and Jiahong Wang* [a, b, c, *]

[a] Shenzhen Institute of Advanced Technology, Chinese Academy of Sciences, Shenzhen 518055, P. R. China

[b] University of Chinese Academy of Sciences Beijing 100049, P. R. China

[c] Department of Physics, Department of Materials Science and Engineering, and Department of Biomedical Engineering, City University of Hong Kong, Tat Chee Avenue, Kowloon, Hong Kong, China

[d] Biomedical Imaging Science and System Key Laboratory, Chinese Academy of Sciences, Shenzhen 518055, P. R. China

‡Y. Da, X. Zhang and C. Peng contributed equally to this work.

*Corrsponding author: (J. H. Wang) jh.wang1@siat.ac.cn

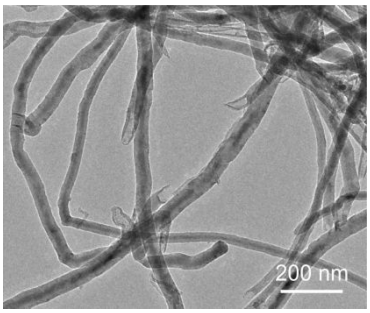

Figure S1. The low- magnification TEM image of conf-BP@CNT.

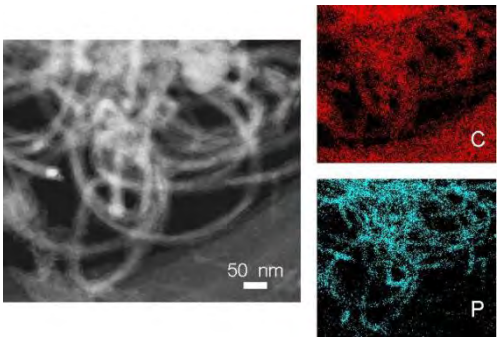

Figure S2. HAADF-TEM image and EDS maps of conf-BP@CNT.

In the as-prepared conf-BP@CNT, the BP nanowires appear in the central part of CNTs.

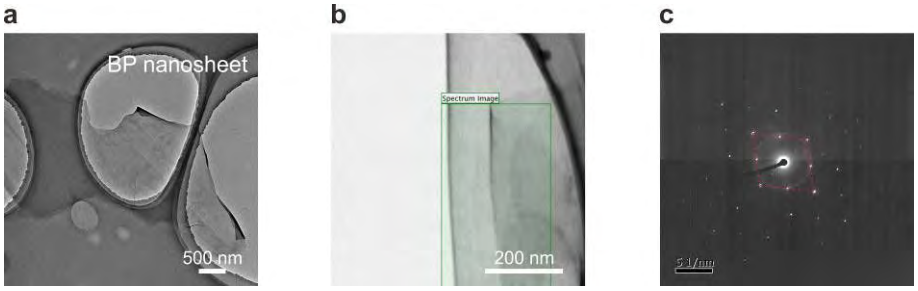

Figure S3. TEM characterization of the BP nanosheet. a) TEM image of the bare BP nanosheet; b) The selected area in the green box is chosen from the BP nanosheet to obtain the EELS spectrum of bare BP; c) The SAED pattern of the BP nanosheet.

In order to investigate the electron energy loss spectroscopy (EELS) spectra of conf-BP and bare BP. The BP nanosheet (Figure S3a) was ultrasonic-exfoliation from bulk BP crystal in ethanol, the bulk BP crystal was growth by chemical vapor transfer (CVT) method.[1, 2] The EELS spectrum of the liquid exfoliated BP nanosheet was detected from the selected green region in Figure S3b. The selected area electron diffraction (SAED) pattern confirms the BP nanosheet is single crystal (Figure S3c).[3, 4]

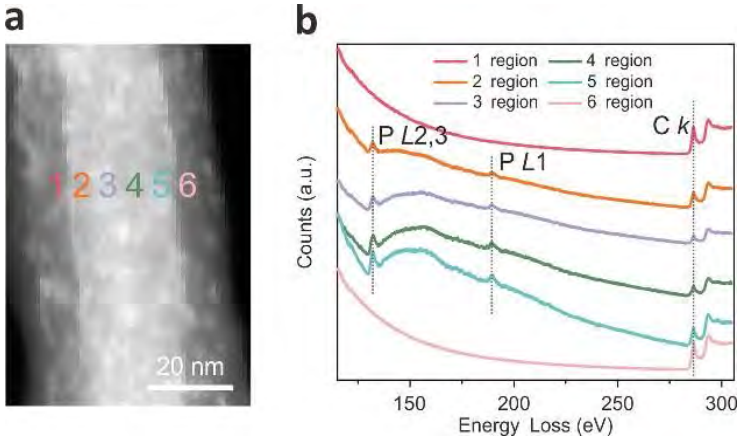

Figure S4. a) HAADF-STEM image of conf-BP@CNT; b) EELS spectra obtained from the six different positions in (a).

The EELS spectra (Figure S4b) obtained from the six areas in Figure S4a show the same carbon k-edge profile. The EELS spectra of the phosphorus $L_{2,3}$-edge and L_1-edge[5,6] are only acquired from the central regions. The results verify the spatially confined distribution of BP.

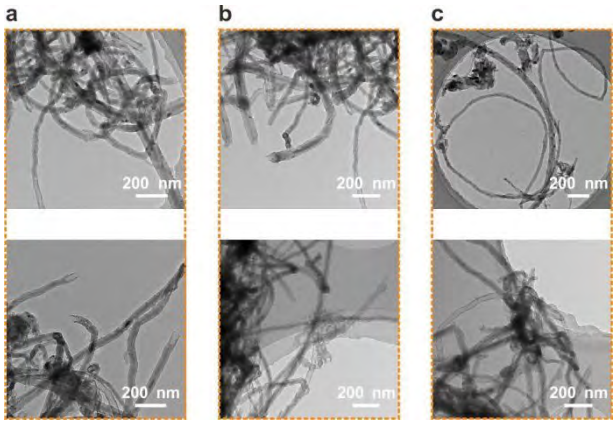

Figure S5. (a−c) TEM images of the samples obtained from three individual experiments.

The conf-BP@CNT nanowires obtained from three individual experiments are investigated by TEM and the images show reliable reproducibility.

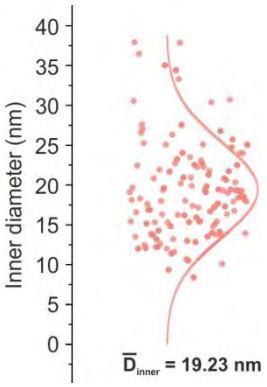

Figure S6. Statistical inner diameter distributions of conf-BP@CNT samples.

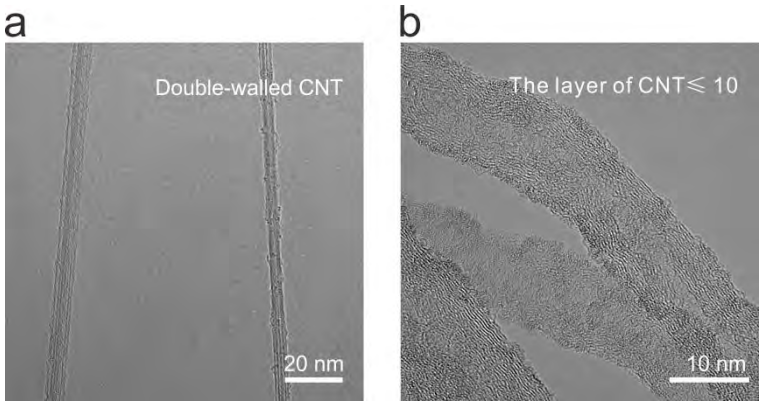

Figure S7. (a) The TEM image of double-walled CNT after confined growth. (b) The TEM image of CNT with less than ten layers after confined growth.

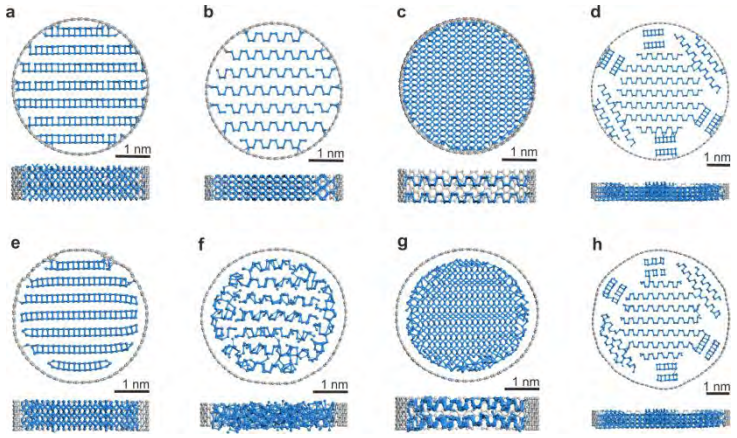

Figure S8. Theoretical analysis of the growth orientation of conf-BP in CNT. (a−d) Structures before relaxation: (a) conf-BP@CNT-*x*, (b) conf-BP@CNT-*y*, (c) conf-BP@CNT-*z*, (d) conf-BP@CNT-*mix*; (e−h) Structures after relaxation: (e) conf-BP@CNT-*x*, (f) conf-BP@CNT-*y*, (g) conf-BP@CNT-*z*, (h) conf-BP@CNT-mix.

The structures before relaxation are shown in Figure S8a−d and no lattice distortion is observed from BP. In the structures after full relaxation, the edges of BP show obvious edge shrinkage and distortion close to the CNT inner wall (Figure S8e−h). Conf-BP@CNT-*y* shows the largest distortion (Figure S8f).

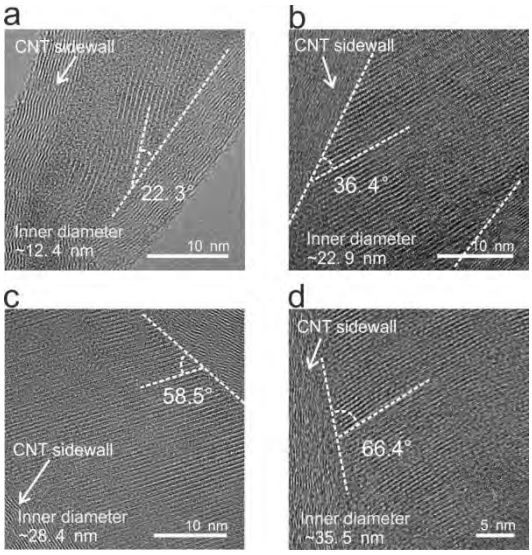

Figure S9. (a-d) The TEM images show that in the CNTs with different inner diameters of 12.4, 22.9, 28.4, and 35.5 nm, conf-BP grows at different angles of 21.2˚, 36.4˚, 58.5˚, and 66.4˚, respectively.

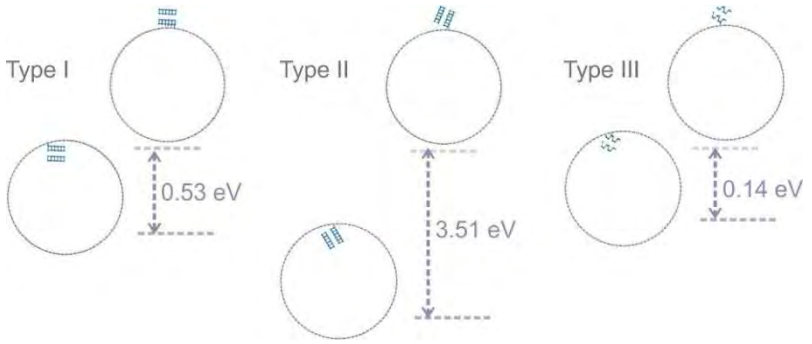

Figure S10. Three simulated configurations of BP fragments composed of the CNT and corresponding formation energy difference between the inner wall loading model and outer wall loading model. In Type I, the basal plane of the BP fragment is attached to the CNT. In Type II, the armchair edge of the BP fragment is connected to the CNT. In Type III, the zigzag edge of the BP fragment is connected to the CNT. All configurations consider BP fragments deposited on the inner wall or outer wall of CNT.

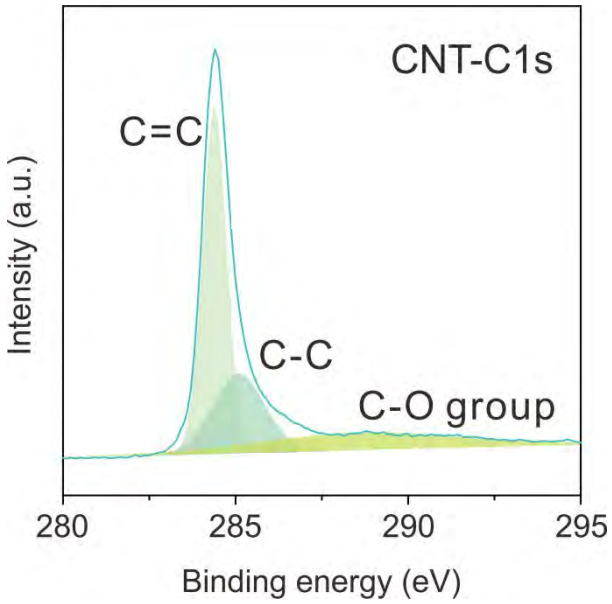

Figure S11. The XPS C1s spectra analysis of CNT.

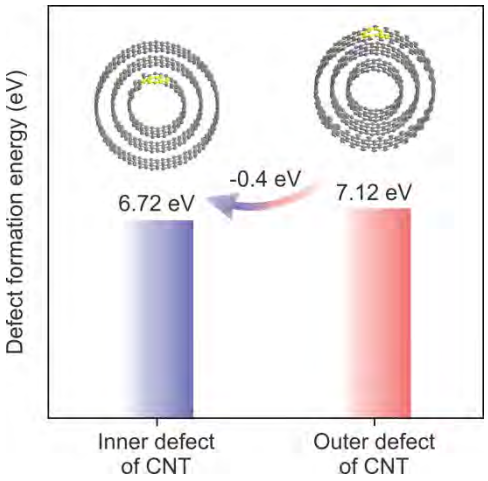

Figure S12. The formation energy of defects at inner/outer of CNT.

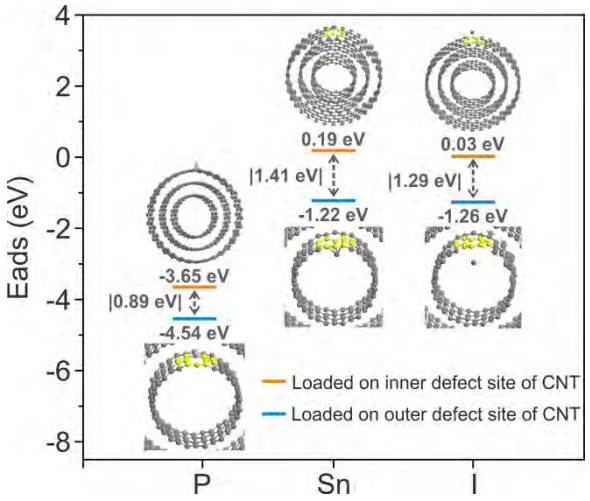

Figure S13. The energy profiles of P, Sn, I elements incorporated with of at inner/outer defects of CNT.

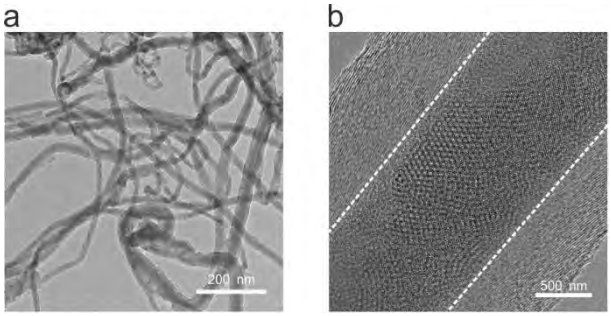

Figure S14. (a) The TEM image of high-temperature treated conf-BP@CNT in which the filling filled substance is not removed; (b) The HRTEM of conf-BP@CNT obtained from (a), in which the BP lattice is mismatch.

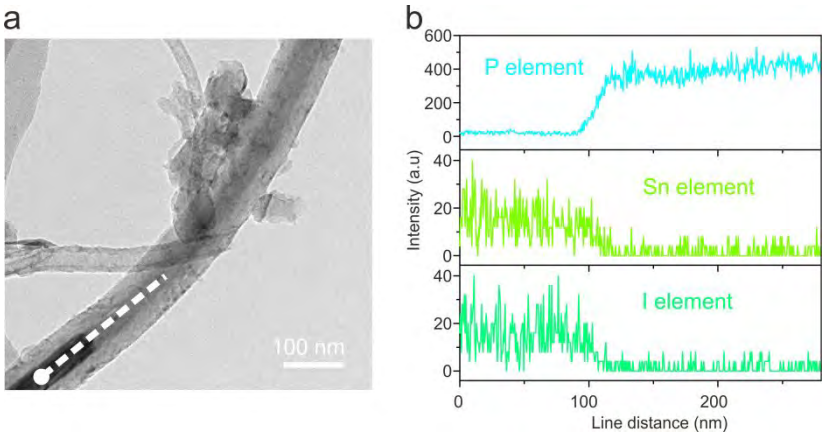

Figure S15. (a) TEM image of conf-BP@CNT; (b) Profile EDS mapping of conf-BP@CNT from dotted white line in (a).

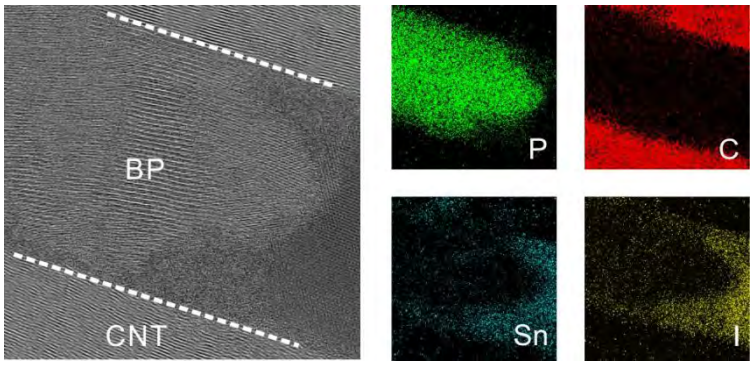

Figure S16. HRTEM image and EDS mapping of growth interface in conf-BP@CNT.

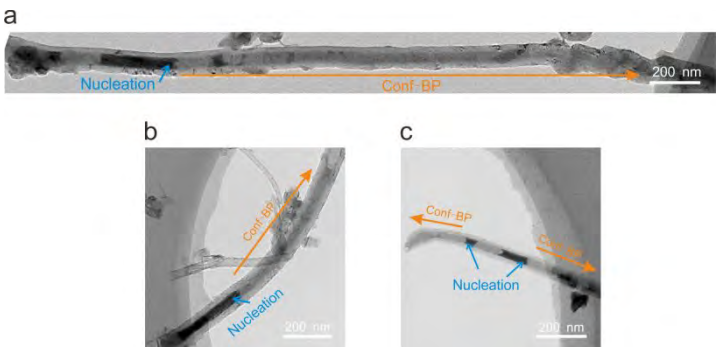

Figure S17. Nucleation sites of conf-BP in CNT. (a, b) TEM images of conf-BP@CNT in which the nucleation site is close to the end of CNT; (c) TEM image of conf-BP@CNT in which the two nucleation sites are near the end of CNT.

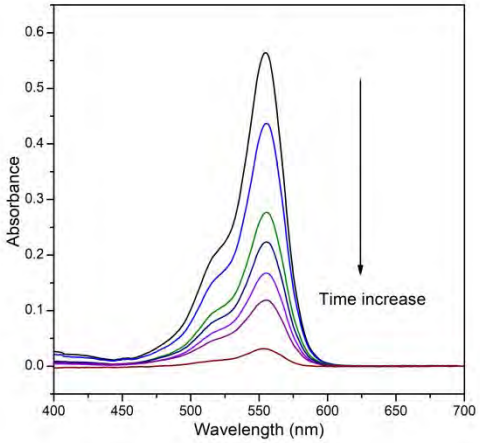

Figure S18 UV-vis absorption spectra of RhB for conf-BP@CNT at different irradiation time.

References

(1) Nilges, T.; Kersting, M.; Pfeifer, T. A fast low-pressure transport route to large black phosphorus single crystals. *J. Solid State Chem.* **2008**, *181*, 1707−1711.

(2) Köpf, M.; Eckstein, N.; Pfister, D.; Grotz, C.; Krüger, I.; Greiwe, M.; Hansen, T.; Kohlmann, H.; Nilges, T. Access and in situ growth of phosphorene-precursor black phosphorus. *J. Crystal Growth* **2014**, *405*, 6−10.

(3) Wu, F.; Xie, A.; Sun, M.; Jiang, W.; Zhang, K. Few-layer black phosphorus: A bright future in electromagnetic absorption. *Mater Lett.* **2017**, *193*, 30−33.

(4) Smith, J. B.; Hagaman, D.; Ji, H. F. Growth of 2D black phosphorus film from chemical vapor deposition. *Nanotechnology* **2016**, *27*, 215602.

(5) Xu, F.; Ge, B.; Chen, J.; Nathan, A.; Xin, L. L.; Ma, H.; Min, H.; Zhu, C.; Xia, W.; Li, Z.; Li, S.; Yu, K.; Wu, L.; Cui, Y.; Sun, L.; Zhu, Y. Scalable shear-exfoliation of high-quality phosphorene nanoflakes with reliable electrochemical cycleability in nano batteries. *2D Mater.* **2016**, *3*, 025005.

(6) Yasaei, P.; Kumar, B.; Foroozan, T.; Wang, C.; Asadi, M.; Tuschel, D.; Indacochea, J. E.; Klie, R. F.; Salehi-Khojin, A. High-quality black phosphorus atomic layers by liquid-phase exfoliation. *Adv. Mater.* **2015**, *27*, 1887−1892.